Energy Proceedings
Vol 33, 2023
ISSN 2004-2965

Molecular Simulation of Adsorption and Flow of Carbon Dioxide in Kaolinite Pores

Guodong Sun [1], Yi Zhang [2*], Mingkun Chen [3], Jingru Zhang [4], Lanlan Jiang[*]

1 Key Laboratory of Ocean Energy Utilization and Energy Conservation of Ministry of Education, School of Energy and Power Engineering, Dalian University of Technology, Dalian 116024, China;

2 Key Laboratory of Ocean Energy Utilization and Energy Conservation of Ministry of Education, School of Energy and Power Engineering, Dalian University of Technology, Dalian 116024, China;

(*Yi Zhang: zhangyi80@dlut.edu.cn, *Lanlan Jiang:lanlan@dlut.edu.cn)

ABSTRACT

With the rapid development of China's economy, a series of environmental problems have emerged, and the large-scale emission of CO_2 has become the main cause of global warming. Carbon capture, utilization, and storage (CCUS) is an important technological means to address climate change. The technology mainly captures CO_2 in the energy production process and converts it into useful products or safely stores it in underground reservoirs, thereby reducing the concentration of CO_2 in the atmosphere. CO_2 storage technology, as an important part of carbon neutrality, has become the key to solving the problem of carbon emissions. Shale clay minerals, as a key site for CO_2 geological storage, provide a large surface area and a large number of pores for adsorption, but the adsorption mechanism and the transport law of CO_2 in the pores during storage still require extensive research. First, the Monte Carlo method was used to simulate the adsorption characteristics of CO_2 in kaolinite pores. The adsorption configuration was established using the molecular simulation software Lammps, and the changes in CO_2 density, isothermal adsorption curve, and CO_2 potential energy distribution in kaolinite pores were analyzed. The main factors affecting CO_2 adsorption and the reasons for the differences in adsorption were comprehensively analyzed. Secondly, based on the research on adsorption characteristics, molecular dynamics method was used to carry out simulation research on supercritical CO_2 flow during adsorption. During the flow process, the potential energy of CO_2 adsorbed on the kaolinite wall changed, causing desorption. Moreover, the larger the pore size, the greater the degree of desorption. In addition, slip occurred at the kaolinite wall during supercritical CO_2 flow, resulting in slip length. With the increase of driving force, the slip length gradually increased, which was due to the decrease of the wall resistance to flow caused by the decrease of CO_2 density in the first adsorption layer with the increase of driving force. Temperature changes also affected the CO_2 slip length. When the temperature rose, the movement of CO_2 molecules became more intense, the curvature radius of the flow curve gradually increased, and the slip length calculated increased with the increase of temperature. At the same time, the increase in temperature caused the potential energy of CO_2 to increase, and the macroscopic behavior of CO_2 molecules became less likely to be adsorbed. On the other hand, when the temperature decreased, the potential energy of CO_2 decreased, and the difference in potential energy between CO_2 molecules and the wall increased, making CO_2 molecules more easily adsorbed and increasing the adsorption amount.

Keywords: CCUS, GCMC, MD, Adsorption, $scCO_2$

NONMENCLATURE

Abbreviations	
APEN	Applied Energy
Symbols	
n	Year

This is a paper for International CCUS Conference 2023 (ICCUSC2023), April 14-15, 2023, Beijing, China.

1. INTRODUCTION

During the Industrial Revolution, the large amount of CO_2 generated caused the Earth's temperature to rise by about 1.5°C from the pre-industrial period to present day[1]. CO_2, as the main component of greenhouse gases, leads to an exacerbation of the global greenhouse effect, causing a series of environmental problems[2, 3]. The Paris Agreement reached a consensus to control global temperature rise to no more than 2°C and to strive for below 1.5°C. Achieving this goal requires joint efforts from all countries, and the Chinese government has made a solemn commitment to the world to reach the "peak" of carbon emissions before 2030 and to achieve "carbon neutrality" before 2060. CO_2 capture, utilization, and storage (CCUS) have been recognized as the main way to solve global climate warming[4]. The main methods for achieving CO_2 storage include geological storage, ocean storage, and chemical storage, among which geological storage and ocean storage are mainly used for storing CO_2 in a supercritical state. Currently, the main types of reservoirs suitable for CO_2 storage include saline aquifers, depleted oil and gas reservoirs, and coal seams[5, 6]. Ku, HC analyzed the mechanism of CO_2 ocean storage and proposed a plan to improve oil recovery, and also discussed the economy of offshore CCS. In terms of mineral storage, Saran, R. K[7] addressed the slow molecular dynamics phenomenon in direct mineral storage and used an indirect method with a multi-step carbonation route to dissolve and precipitate, making indirect mineral storage an effective choice for CO_2 storage. The mechanism of CO_2 storage is complex, and McDermott, C[8] established an empirical stress function to evaluate the geological stability of CO_2 storage through static analysis and dynamic simulation analysis. When the temperature of CO_2 exceeds 31°C and the pressure exceeds 7.38 MPa, it can be compressed into a supercritical state[9]. Supercritical CO_2 has properties similar to those of liquids, with a density close to that of fluids, zero interfacial tension, viscosity close to that of gases, and diffusion coefficients greater than those of gases. Its formation mechanism can be used as a condition for finding the best reservoir. In the process of CO_2 storage, the stability of the reservoir is an important indicator for measuring the quality of storage; otherwise, CO_2 leakage into the atmosphere can threaten human life[10-13]. The pore size and structure of the reservoir are the key factors affecting whether supercritical CO_2 can be effectively stored, directly affecting the amount of CO_2 adsorbed in the pore and the judgment of the strength of the adsorption on the pore wall[14-16].

As an important reservoir in geological storage, shale's clay components mainly include kaolinite, illite, and montmorillonite. In regards to adsorption in shale clay minerals, Ross, DJK, and others[17] studied the effects of shale structure and composition on CH_4 adsorption in the western sedimentary basin of Canada. They demonstrated that clay minerals can adsorb gas into their internal pores, and the amount of adsorption depends on the porosity of the clay. Clay minerals have single pore diameters less than 10 nm, while other non-clay minerals such as quartz-bearing shale have no micropores or mesopores. Therefore, studying the adsorption mechanism in clay pores is of great significance for geological storage.

Research in molecular simulation is typically focused on high-pressure ranges. However, this article investigates the adsorption process of CO_2 from the gas state to the supercritical state within a pressure range of 0.1-35 MPa. Additionally, non-equilibrium molecular dynamics simulations were employed to investigate the leakage behavior of supercritical CO_2 during CO_2 storage.

2. MATERIAL AND METHODS

2.1 Adsorption model construction

2.1.1 Adsorption model of Kaolin-CO_2

Kaolinite, as the main component of clay, has a molecular formula of . Its crystal belongs to the triclinic system and has a layered structure, with the upper and lower layers connected by bridging oxygen atoms between aluminum octahedra and silicon tetrahedra[5, 18, 19]. The crystal parameters used in this study are from Bish et al[5]. The initial unit cell is shown in Figure 2.1, with lattice constants of 5.15 Å, 8.93 Å, and 7.38 Å in the three directions, and angles of 91.930°, 105.04196°, and 89.791° in the three directions.

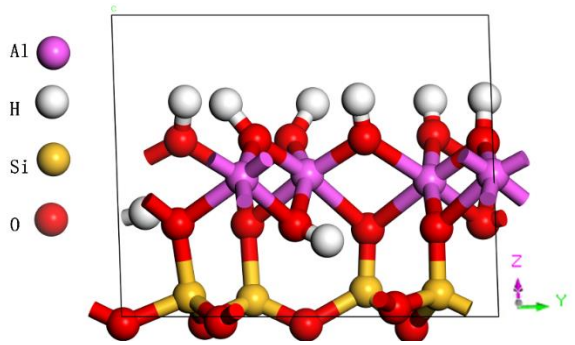

Fig. 2.1. Initial cell model of kaolinite

Due to differences in burial depth of clay minerals, there are differences in pressure and internal pressure during the sealing process. In this section, simulation conditions were selected with a pressure range of 0.1-35

MPa and a temperature of 350 K. Figure 2.2 shows the initial adsorption model of CO_2 in a 1 nm pore of kaolinite. The kaolinite cell was expanded by 8×6×6, and the upper and lower pore walls were both the (001) crystal surface of kaolinite.

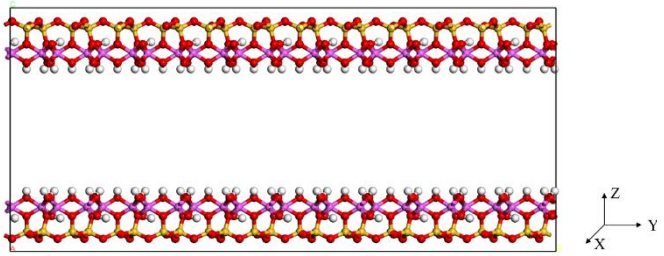

Fig. 2.2. Initial adsorption model of carbon dioxide in 1 nm pores of kaolinite

To investigate the effect of temperature on CO_2 adsorption on kaolinite, a 6 nm kaolinite (001) pore model was constructed to simulate the adsorption characteristics at three temperatures of 350 K, 370 K, and 390 K. The pore model was based on the model in Figure 2.2, with the pore size increased to 6 nm. Additionally, the adsorption characteristics of CO_2 on kaolinite at 350 K and 20 MPa were also studied in 1 nm, 2 nm, 4 nm, and 6 nm pores based on the model in Figure 2.2.

2.1.2 Simulation details of adsorption

The MD+GCMC combined method was used to simulate CO_2 adsorption in the system. The simulation time step was 1 femtosecond, and the potential cutoff radius was 1.5 nm. The total running time was 2 ns. Due to the changing number of particles in the system, the NVT ensemble was used for temperature control, and the Nose-Hoover algorithm was used. During the running process, 100 GCMC exchanges were performed every 100 steps, and approximately 0 GCMC moves were performed every 100 steps. The maximum distance of MC process movement was 0.5 Å. The shake algorithm was used for CO_2 molecules in the system. In LAMMPS, besides directly specifying the chemical potential, the pressure keyword can be used to indirectly set the chemical potential of the large system. In this study, the indirect method of specifying the chemical potential through pressure was used, as different pressures were needed to investigate the effect on CO_2 adsorption. The fugacity coefficient also needed to be set, with a default value of 1 in LAMMPS. During the simulation, the density of CO_2 was directly outputted as it varied with different pressures, temperatures, and pore sizes.

2.2 $scCO_2$ flow simulation

2.2.1Kaolinite-$scCO_2$ flow model

To simulate the flow behavior of supercritical CO_2 in kaolinite pores under different conditions, it is necessary to construct a kaolinite model and determine the number of supercritical CO_2 molecules in the pores under different temperature and pressure conditions. In this chapter, the final adsorption configuration of a 6nm kaolinite pore at 350 K and 20 MPa obtained in Section 2.1 was used directly as the initial flow model, as shown in Figure 2.3. The (001) surface is present on both the upper and lower surfaces of the kaolinite pore, and the pore sizes are 4.12 nm, 5.36 nm, and 8.75 nm, respectively. The Clayff[20] force field was used to describe the kaolinite pores, which is suitable for studying the interaction between clay and fluid. Only the hydroxyl bond stretching term is considered for kaolinite in this force field, and the EPM2[21] force field parameters are used for supercritical CO_2. The kaolinite-supercritical CO_2 flow model is divided into bonded and non-bonded interactions, with the bonded interactions described by Coulomb potential and the non-bonded interactions described by van der Waals and Coulomb forces. During the simulation, the walls on both sides of the kaolinite are fixed, and the CO_2 molecules are treated as rigid bodies with no internal degrees of freedom.

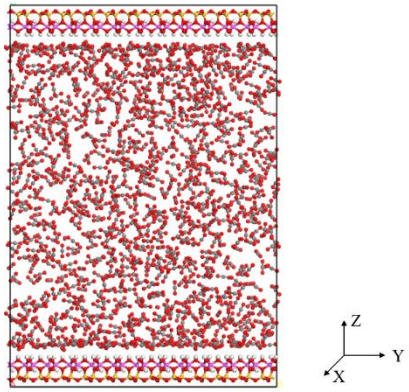

Fig. 2.3 Initial Configuration of kaolinite 6nm Po re Flow

2.2.2 $scCO_2$ Simulation details of flow modeling

During the flow process, the non-equilibrium molecular dynamics method was used with periodic boundary conditions in all three directions. The stretching of the hydroxyl bonds in the kaolinite and the stretching of the C=O bond and bending of the O=C=O angle in the CO_2 molecule were described using harmonic potentials. The simulation time step was 1 femtosecond, and the potential energy cutoff radius was set to 1.5 nanometers. Initially, the CO_2 molecules were equilibrated in the NVT ensemble for 5 nanoseconds

using the Nose-Hoover thermostat. In addition, a driving force was applied to each atom in the CO_2 phase along the y direction to induce flow. It should be noted that when driving the CO_2, the y-component should be excluded from the temperature control range, otherwise, the temperature may deviate from the expected value, leading to significant errors in the results. Statistical analysis was carried out after the model reached the expected temperature. A slice thickness of 0.2 angstroms was used for analysis along the Z direction, with file outputs generated every 20 picoseconds. The total statistical analysis time was 5 ns, and the total simulation time was 10 ns.

2.3 Force field parameters and functions

The total potential energy (E_{total}) of a molecule includes both the bond energy and non-bond energy. Bond energy refers to the internal forces within a molecule, while non-bond energy refers to the interactions between molecules. The internal forces within a molecule include bond stretching (E_{bond}) and angle bending potential energy (E_{angle}), while the intermolecular forces include Coulombic forces (E_{coul}) and van der Waals forces (E_{vdw}). The relationship between the total potential energy, bond energy , and non-bond energy can be expressed as follows in a formula(2.1):

$$E_{total} = E_{bond} + E_{angle} + E_{coul} + E_{vmd} \quad (2.1)$$

When calculating the bond stretching potential energy between molecules, a harmonic potential energy function is often used, which can be expressed mathematically as Equation (2.2):

$$E_{bond} = \frac{1}{2} k_{ij} (r_{ij} - r_0)^2 \quad (2.2)$$

In this equation, k_{ij} represents the bond constant, which is a measure of the strength of the bond and is inversely proportional to the ease with which the bond can be stretched. r_{ij} represents the distance between the atoms involved in the bond, while r_0 represents the equilibrium bond length, which is the optimal distance between the atoms in the bond.

Due to the small vibrational motion of bond angles, a harmonic potential energy function is also used when calculating the angle bending potential energy, which can be expressed mathematically as Equation (2.3):

$$E_{angle} = \frac{1}{2} k_{ijk} (\theta_{ijk} - \theta_0)^2 \quad (2.3)$$

In this equation, k_{ijk} represents the angle constant, which is a measure of the rigidity of the angle and is directly proportional to the resistance of the molecule to changes in angle. θ_{ijk} represents the angle between the atoms involved in the bond, while θ_0 represents the equilibrium angle, which is the optimal angle between the atoms in the bond in the absence of external forces.

The intermolecular van der Waals interaction energy between molecules is often modeled using the classical Lennard-Jones potential energy function, which can be expressed mathematically as Equation (2.4):

$$E_{vdw} = 4\varepsilon_{ij}\left[\left(\frac{\sigma_{ij}}{r_{ij}}\right)^{12} - \left(\frac{\sigma_{ij}}{r_{ij}}\right)^{6}\right] \quad (2.4)$$

The equation consists of two terms: the first term represents the short-range repulsive interaction, which dominates when the distance between the atoms is smaller than r_{ij}; the second term represents the long-range attractive interaction, which dominates when the distance between the atoms is larger than r_{ij}. In the equation, r_{ij} is the distance between the atoms, ε_{ij} is the energy difference between the potential energy minimum and the energy at infinite separation, and σ_{ij} is the distance at which the potential energy is zero.

The electrostatic force between molecules is expressed by Coulomb's law as shown in equation (2.5):

$$E_{coul} = \frac{q_i q_j}{4\pi\varepsilon_0 \varepsilon_{ij}} \quad (2.5)$$

Kaolinite(CLAYFF force field[20])			
Atom	q(e)	ε(kcal/mol)	δ(Å)
ao	1.575	1.33e-6	4.7943
st	2.1	1.84e-6	3.7064
ob	-1.05	0.1554	3.5532
oh	-0.95	0.1554	3.5532
ho	0.425	0.0	0.0
oc	0.6512	0.0559	2.757
co	-0.3256	0.1600	3.033
Bonds	kij/(kcal/mol/Å)		Bo(Å)
oh-ho	554.1349		1.0

CO_2(Flexible EPM2 force field[21])			
Atom	q(e)	ε(kcal/mol)	δ(Å)
CC	0.6512	0.0559	2.757
OC	-0.3256	0.1600	3.033
B0(Å)		1.149	
φ0		180	
K_{ij}/(kcal/mol/Å^2)		2.56	
K_{ijk}/(kcal/mol/rad^2)		295.41	

3. RESULTS

3.1 Analysis of Adsorption Simulation Results

3.1.1 Impact of Pressure on Adsorption

Figure 3.1 shows the isothermal adsorption curve of CO_2 in a 1 nm pore at a temperature of 350 K. The total adsorption amount is the number of CO_2 molecules in the fixed pores of kaolin obtained by Monte Carlo method calculation at a certain pressure and temperature; the bulk content refers to the CO_2 molecules theoretically calculated in the fixed volume of the kaolin pore at the corresponding pressure and temperature; and the excess adsorption amount refers to the number of CO_2 molecules obtained by subtracting the total adsorption amount from the bulk content at the corresponding pressure and temperature in the kaolin pore. It can be observed from the figure that the total adsorption amount of CO_2 increases rapidly with pressure in the range of 0.1-6 MPa, but as the pressure gradually increases, the increasing trend of the total adsorption amount slows down and tends to flatten. This is because CO_2 molecules in a 1 nm kaolin pore are subject to the dual effects of the potential energy of the two wall surfaces. As the pressure gradually increases, the number of CO_2 molecules in the pore increases significantly, but when the pressure further increases, the increasing trend of the total adsorption amount slows down due to the fixed pore of the kaolin. The excess adsorption amount of CO_2 shows an upward trend first and then gradually decreases with the gradual increase of pressure, and it is positive in the range of 0.1-20 MPa, which also reflects the adsorption of kaolin on CO_2. From Figure 3.1, it can be seen that the excess adsorption amount shows an upward trend in the range of 0.1-10 MPa, which is due to the strong adsorption of kaolin on CO_2 caused by the adsorption of CO_2 on the adsorption sites on the kaolin 001 crystal surface. However, in the range of 10-20 MPa, with the further increase of pressure, the number of CO_2 molecules in the pore approaches that in the bulk, leading to a gradual decrease in excess adsorption amount.

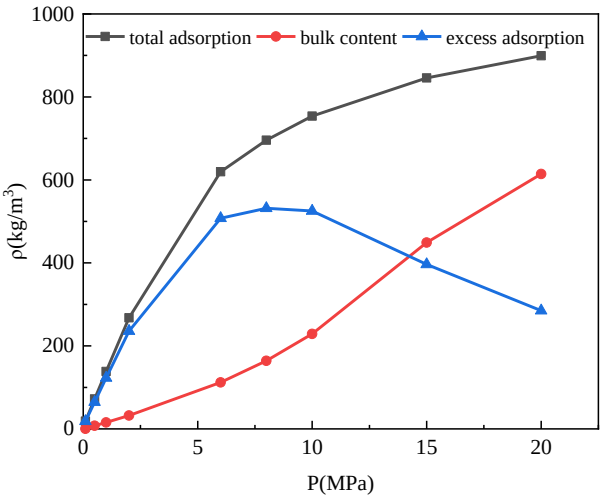

Fig. 3.1 Isothermal adsorption curve of carbon dioxide in 1nm pores of kaolinite

Figure 3.2 shows the density distribution curves of CO_2 in a 1 nm pore of kaolinite at 350 K and nine pressures ranging from 0.1 MPa to 20 MPa. The density distribution curve of CO_2 exhibits a bimodal trend due to the strong adsorption of CO_2 by the kaolinite on both sides of the pore. The adsorption layer appears near the pore walls, where CO_2 molecules aggregate. In Figure 3.2, two adsorption layers are observed within the 1 nm pore, with a thickness of approximately 0.38 nm for a single layer and a total thickness of 0.76 nm for the entire CO_2 region. This thickness is less than the width of the 1 nm pore due to the van der Waals forces between the CO_2 molecules and the atoms on the kaolinite (001) surface. Additionally, the figure shows that as the pressure increases, the peak of the adsorption layer gradually increases, but the rate of increase decreases. This is because as the adsorption sites in the pore are gradually occupied, the CO_2 molecules adsorbed at higher pressures can only occupy weaker adsorption sites. Figure 3.2 also indicates that CO_2 molecules exist only in the adsorbed state within the 1 nm pore of kaolinite, and there are no free CO_2 molecules present.

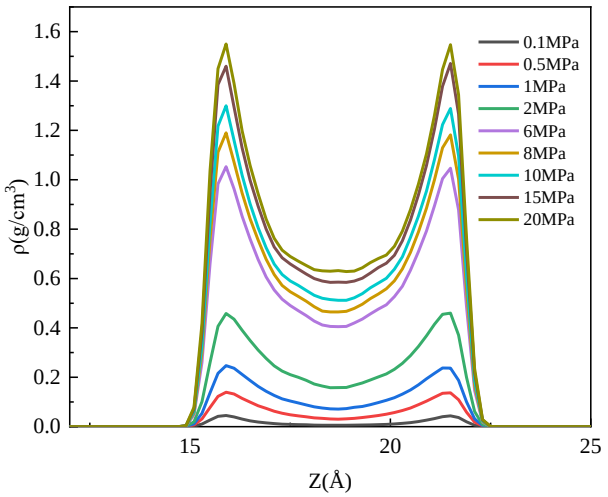

Fig. 3.2 Density distribution curve of carbon dioxide in 1nm pores of kaolinite3.1.2 The Influence of Temperature on Adsorption

To investigate the effect of temperature on the adsorption of CO_2 by kaolinite, a 6 nm kaolinite (001) surface pore model was constructed to simulate the adsorption characteristics at three temperatures: 350 K, 370 K, and 390 K. Figure 3.3 shows the isothermal adsorption density curves of CO_2 in the 6 nm pore at the three temperature conditions. From the figure, it can be seen that the adsorption of CO_2 at all three temperatures increases first and then tends to flatten out as the pressure increases. Within the pressure range of 0.1-15 MPa, the isothermal adsorption density curve of CO_2 increases most rapidly with increasing pressure, because there are more adsorption sites in the 6 nm pore of kaolinite, and the number of adsorbed CO_2 molecules increases significantly within a certain pressure range. As the temperature increases, the value of the isothermal adsorption density curve of CO_2 decreases, indicating that the adsorption of CO_2 in the kaolinite pore decreases with increasing temperature, and the temperature increase causes the desorption of CO_2.

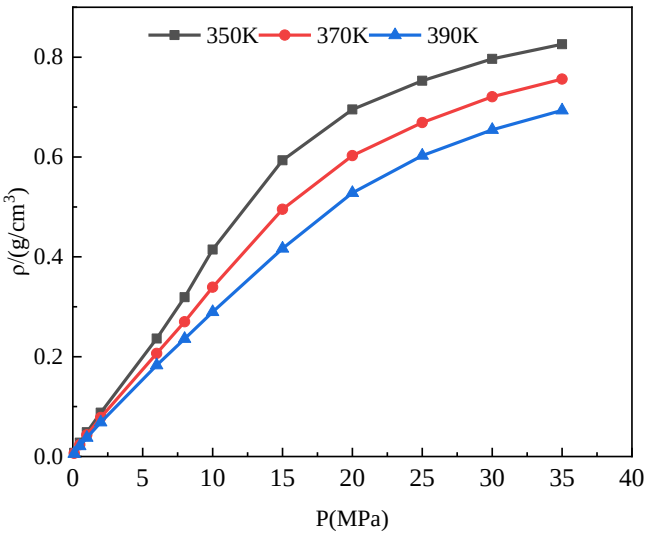

Fig. 3.3 Total adsorption density of CO_2 in 6nm pores of kaolinite

As shown in Figure 3.3, increasing the temperature reduces the CO_2 isothermal adsorption density, that is, the amount of adsorption decreases. However, the specific manner in which the density decreases in the system is still unknown. Further obtaining the CO_2 density distribution curves at the three temperatures of 350 K, 370 K, and 390 K, as shown in Figure 3.4, it can be seen that two adsorption layers are formed in the 6 nm pore at all three temperatures. In addition, the density of the remaining CO_2 molecules in the free state remains basically the same. This is because the free region is far away from the wall and is negligible in terms of the adsorption effect of the kaolin wall. As the temperature increases, both the adsorption layer density and the free state density decrease significantly. Not only the adsorption region is affected by the temperature, but also the CO_2 molecules in the free region are clearly affected by the temperature.

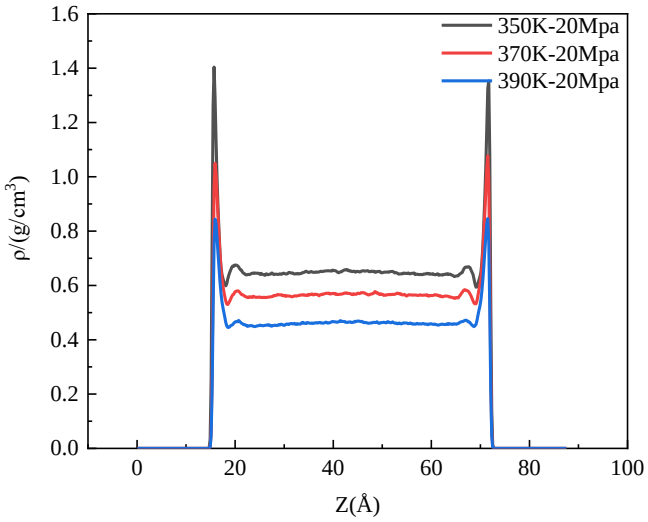

Fig. 3.4 CO_2 Adsorption Density Density Curve at Different Temperatures in kaolinite 6nm Pores

3.1.3 The Effect of Pore Size on Adsorption

This section investigates the adsorption characteristics of CO_2 in high-alumina zeolite pores with diameters of 1 nm, 2 nm, 4 nm, and 6 nm at 350 K. As shown in Figure 3.5(a), the amount of CO_2 adsorption increases with increasing pore size, and the adsorption isotherms for CO_2 in each pore group decrease with increasing pressure. As the pressure increases from 0-10 MPa, the amount of CO_2 adsorption in different pore sizes increases significantly, while the slope of the CO_2 isotherm adsorption curve decreases in the pressure range of 10-20 MPa. This phenomenon is also evident in Figure 3.5(b), where the excess adsorption amount gradually increases within the pressure range of 0-10 MPa and reaches a peak at 10 MPa, after which the excess adsorption amount gradually decreases within the pressure range of 10-20 MPa, indicating that the adsorption gradually reaches saturation. By comparing the CO_2 isotherm adsorption curves in Figure 3.5(a), the total adsorption in the 1 nm pore size is higher than that in the 2 nm and 6 nm pores, and the adsorption in the 2 nm pore size is higher than that in the 6 nm pore size. This is because in smaller pores, CO_2 is significantly affected by wall potential energy, and CO_2 molecules in the pores are subjected to the superposition of wall potential energy, resulting in lower potential energy and more CO_2 being adsorbed on the wall.

Figure 3.5(c) shows the CO_2 adsorption density curves obtained for different pore sizes of high-alumina zeolite at 350 K and 20 MPa. As can be seen from the figure, there is only one adsorption layer in the 1 nm pore size, and CO_2 molecules exist only in the adsorbed state, with no free CO_2 molecules present. In the 2 nm, 4 nm, and 6 nm pores, there are two adsorption layers, and both adsorbed and free CO_2 molecules are present in the pores. The adsorption layer height in the 1 nm and 2 nm pores is significantly higher than that in the 4 nm and 6 nm pores, which is due to the significant adsorption effect of the wall on CO_2 molecules in the smaller pores. As shown in the figure, the adsorption layer heights in the 4 nm and 6 nm pores are the same, and the peak and free layer heights are similar. At this point, the adsorption is no longer affected by pore size, and only the amount of bulk CO_2 increases.

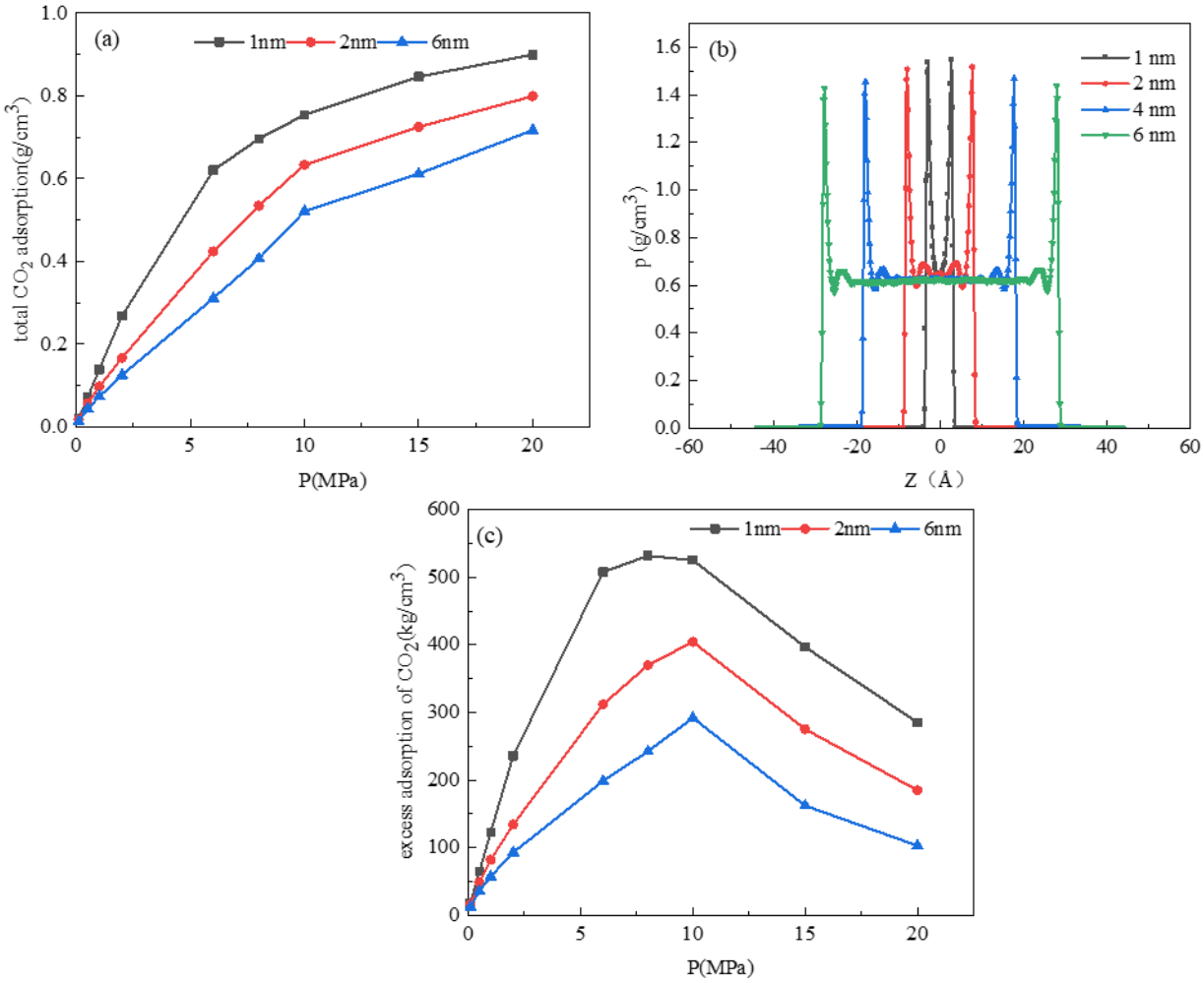

Figure 3.5 the isothermal adsorption curves (a), excess adsorption (b), and density curves (c) of CO_2 in different pores of kaolinite.

3.1.4 Potential Energy Distribution and Normalization

Further analysis was carried out on the potential energy distribution of CO_2 in the 1 nm pore of kaolin at a fixed temperature of 350 K and in the pressure range of 0.1-35 MPa, and the adsorption potential energy values and probability density at that energy level were obtained as shown in Figure 3.6(a). The peak value of the probability density can be used to determine whether adsorption has reached saturation. At 0.1 MPa, the CO_2 potential energy Poisson distribution showed a bimodal shape. This is because at lower adsorption pressures, low potential energy CO_2 molecules are mainly adsorbed on the strongly adsorbing sites on the surface of the kaolin crystal, while the remaining high potential energy CO_2 molecules are weakly adsorbed due to the weak adsorption on the surface, resulting in a bimodal distribution. It can also be seen that the peak value of low potential energy CO_2 molecules is higher than that of high potential energy CO_2 molecules. In the pressure range of 0.5-35 MPa, the CO_2 potential energy Poisson distribution was unimodal. As the pressure increased, the number of CO_2 molecules in the center of the pore increased significantly, and the interaction between molecules became more obvious. This interaction caused the high potential energy CO_2 molecules in the center of the pore to transition to a low potential energy state. This is also the reason why the CO_2 Poisson distribution shifted to the low potential energy direction as the pressure increased. Figure 3.6 also shows that as the pressure increased, the peak value of the CO_2 potential energy Poisson distribution first decreased, then increased, and finally stabilized. This is because at low pressures, low potential energy CO_2 molecules mainly exist on the kaolin surface, and low potential energy CO_2 molecules preferentially adsorb on the strongly adsorbing sites. As the pressure further increases, the number of low potential energy CO_2 molecules further

increases, but at this time, the number of strongly adsorbing site CO_2 molecules gradually tends to saturation, and the increasing CO_2 molecules are in the weakly adsorbing sites, causing the peak value of the CO_2 potential energy Poisson distribution to decrease. The CO_2 potential energy Poisson distribution at 30 MPa and 35 MPa in Figure 3.6(a) shows that the peak values of the CO_2 potential energy Poisson distribution at these two pressures are basically the same, and there is some overlap on the left side of the potential energy distribution, indicating that the CO_2 adsorption has reached saturation. The CO_2 potential energy Poisson distribution indirectly explains the reason why the number of CO_2 molecules adsorbed in the kaolin pore under 350 K conditions gradually increased and then tended to saturation with increasing pressure, as shown in Figure 3.4.

According to the normalized CO_2 adsorption distribution corresponding to different potential energies in Figure 3.6(d), which was obtained by normalizing the CO_2 potential energy distribution at different pressures and combining it with the number of CO_2 adsorptions, it can be seen that as the pressure increases, the CO_2 potential energy tends to decrease, which is consistent with the phenomenon shown in Figure 3.6(a). As the CO_2 potential energy decreases, it means that more CO_2 molecules will be adsorbed in the pores. As shown in the figure, as the pressure increases, the peak of the CO_2 potential energy normalized corresponding number of adsorptions gradually increases. However, the difference is that during the transition from 8 MPa to 10 MPa, although the CO_2

Figure 3.6(b) also shows that as the temperature increases, the left peak slightly increases while the right peak decreases. Combining with the CO_2 adsorption number under different potential energies in Figure 3.6(e), it can be seen that increasing the temperature reduces both the adsorbed and free CO_2 molecules, indicating that temperature has an effect on both the adsorbed and free CO_2 molecules.

Figure 3.6(c) further analyzes the changes in CO_2 potential energy in different pores from a molecular dynamics perspective. As shown in the figure, there is only one potential energy peak for CO_2 in the 1 nm pore, while there are two potential energy peaks in the 2 nm, 4 nm, and 6 nm pores. This is consistent with Figure 3.2, where CO_2 molecules exist in the adsorbed state in the 1 nm pore, and as the pore size increases, free-state CO_2 molecules begin to appear, with the lower potential energy corresponding to the adsorbed state and the potential energy decreases further, the normalized peak corresponding to the CO_2 potential energy at 8 MPa is higher than that at 10 MPa. This means that the number of CO_2 molecules adsorbed at 8 MPa pressure is higher than that at 10 MPa, but as shown in Figure 3.2, the CO_2 adsorption density at 8 MPa pressure is lower than that at 10 MPa. The reason for this phenomenon is that the pressure state point is close to the critical state, and the CO_2 density is sensitive to pressure changes, especially in the fluctuations of density. The potential energy distribution and density fluctuations at 8 MPa pressure near the critical state are not positively correlated.

The density fluctuates noticeably with temperature, and the change in CO_2 adsorption with temperature is further analyzed from the perspective of molecular dynamics potential energy. The potential energy distribution of CO_2 at three different temperatures is shown in Figure 3.6(b), where there are two peaks in CO_2 potential energy, with adsorbed CO_2 in the lower potential energy region and free CO_2 in the higher potential energy region. Since the majority of CO_2 molecules in the system are in the free state, the probability peak corresponding to the potential energy of free CO_2 molecules is higher than that of adsorbed CO_2 molecules. As the temperature increases, the Poisson distribution curve of CO_2 potential energy shifts to the right in the direction of increasing potential energy, indicating that the average potential energy of CO_2 as a whole increases with increasing temperature, and CO_2 molecules become less stable. This further demonstrates the promoting effect of temperature on CO_2 desorption from a microscopic perspective.

higher potential energy corresponding to the free state. From Figure 3.6(f), it can be seen that the 1 nm pore has the lowest potential energy, the adsorbed state potential energy in the 2 nm pore is relatively lower than that in the 4 nm and 6 nm pores, and the adsorbed state potential energy in the 4 nm and 6 nm pores is basically the same. As mentioned before, in smaller pores such as the 1 nm pore, the overlapping effect of the kaolin wall leads to a lower potential energy for adsorbed CO_2 molecules, while in larger pores such as the 4 nm and 6 nm pores, the adsorbed CO_2 molecules tend to reach a stable state, and the stable action of the two side walls on the adsorbed CO_2 molecules leads to no change in the adsorbed state potential energy. Combining Figure 3.5(c) with Figure 3.6(c) and (f), it can be seen that as the pore size increases, the number of adsorbed layer molecules changes little, the potential energy peak of the adsorbed

state molecules in Figure 3.6(c) decreases slightly, and the potential energy and peak of free state molecules increase. This is because as the pore size increases, the main increase in the pore is high potential energy free-state CO_2 molecules, while the number of adsorbed state CO_2 molecules changes little, and the proportion of the overall number of molecules decreases.

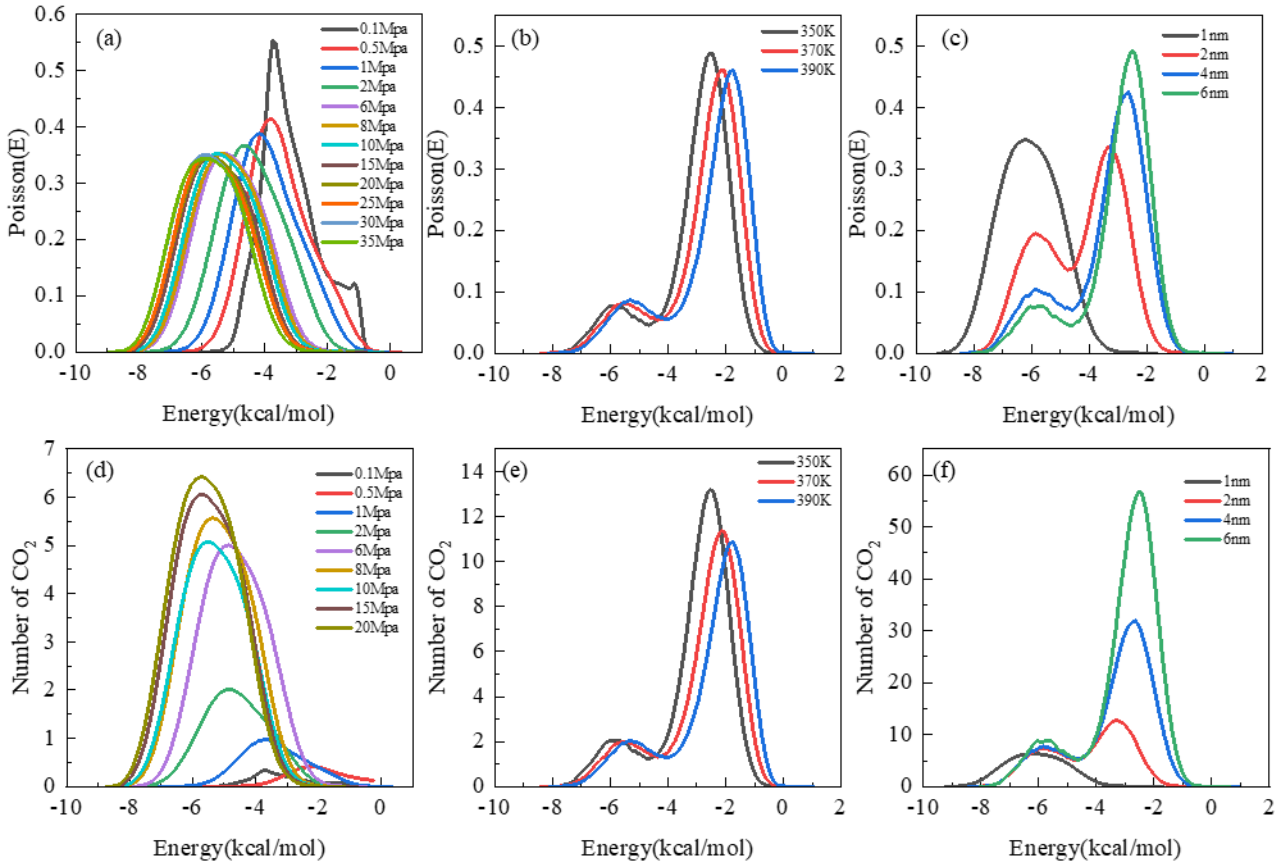

Figure 3.6 Potential energy distribution and normalized CO_2 number distribution of a 1nm kaolinite pore at different pressures, temperatures, and pore sizes.

3.2scCO_2 Analysis of Flow Simulation Results

Monte Carlo method was used to simulate CO_2 adsorption in different pores, under the environment of 350 K and 20 MPa, where CO_2 reached the supercritical state. Non-equilibrium molecular dynamics simulation was further conducted to study the flow behavior of leaked supercritical CO_2 during sequestration. Slip boundary conditions were considered in the microscopic simulation, and the slip length during the flow process was calculated. As the flow of supercritical CO_2 follows the Poisson distribution, the flow viscosity was obtained by fitting the simulation results, and compared with known NIST experimental data to verify the simulation's rationality. The chapter discusses the influence of driving force, temperature, and pore size on the flow behavior of supercritical CO_2.

3.2.1 The Impact of Driving Force on Fluid Flow

As shown in Figure 3.7(a), the density distribution of CO_2 under different driving forces in supercritical state exhibits two adsorption layers and one free layer during the non-equilibrium molecular dynamics flow process. The density in the first adsorption layer is higher than that in the second adsorption layer, which is caused by the different potential energies of CO_2 at different positions. As shown in Figure 3.7(b), the CO_2 potential energy distribution, represented by the potential energy distribution of the carbon atom in CO_2, can explain this phenomenon. The first adsorption layer has lower CO_2 potential energy, which leads to a stronger interaction with the montmorillonite surface and a greater number of CO_2 molecules adsorbed in this layer. The potential energy of CO_2 in the second adsorption layer is higher than that in the first layer, and the distance between the second layer and the montmorillonite surface is relatively greater, resulting in a weaker interaction with

the surface and fewer CO_2 molecules adsorbed in this layer. In Figure 3.7(a), as the driving force increases, the peak value of the wall adsorption decreases, and the greater the driving force, the more obvious the peak value decrease.

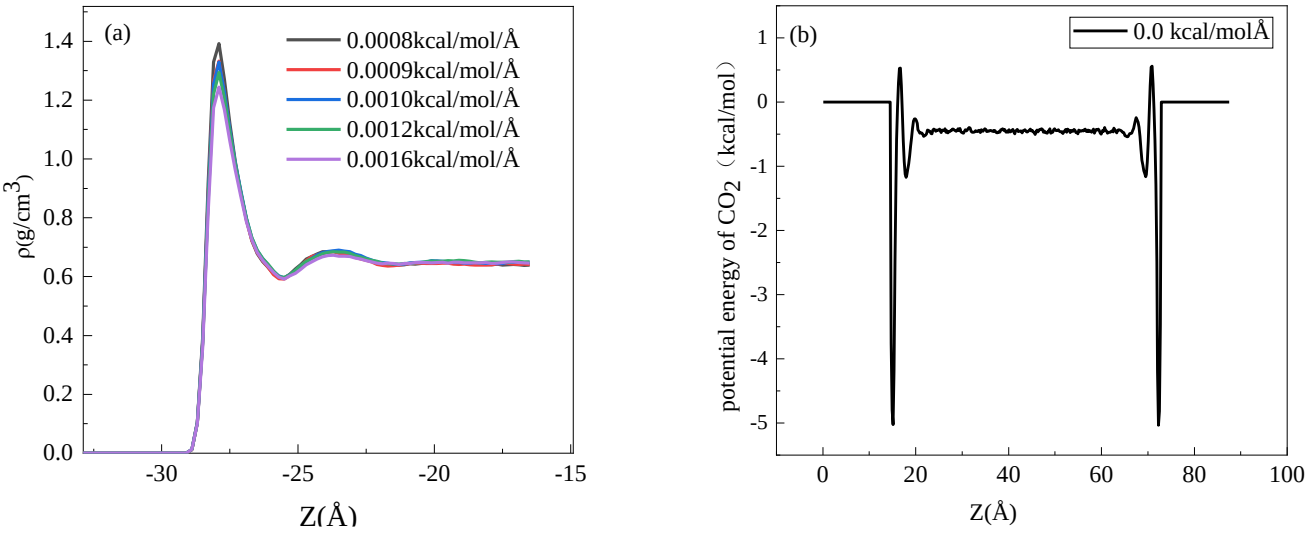

Figure 3.7 Density distribution of $scCO_2$ flow in different forces acting on the 6nm kaolinite pore (a) and static potential energy distribution of $scCO_2$ (b).

Figure 3.8 depicts the velocity distribution of supercritical CO_2 during non-equilibrium molecular dynamics simulation, which shows that the velocity distribution of supercritical CO_2 follows a quadratic curve. As the driving force increases, the curvature radius of the quadratic curve increases, and the velocity of supercritical CO_2 increases. The parabolic curve is symmetrically distributed, and the velocity of supercritical CO_2 molecules farther from the wall surface is higher. Due to the adsorption of the pore walls on supercritical CO_2 molecules, during non-equilibrium molecular dynamics simulation, molecules close to the wall need to overcome this resistance to flow, which is manifested as viscosity. CO_2 molecules far from the wall and close to the center of the pore experience less wall adsorption, resulting in more significant changes in their velocity.

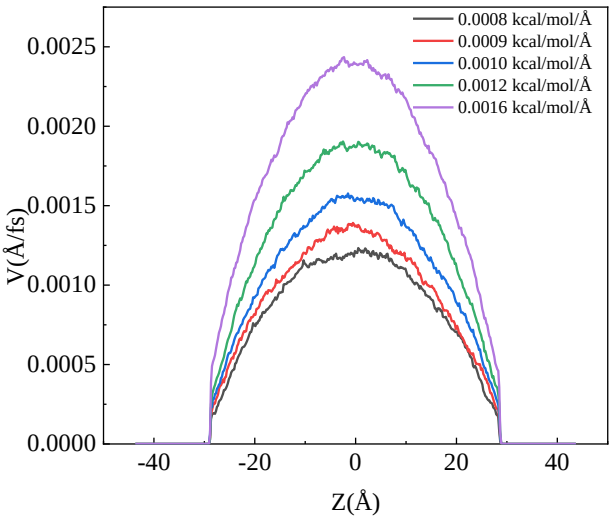

Fig. 3.8 Distribution of Carbon Dioxide Velocity under Different Forces in kaolinite 6nm Pore

The coefficients of the quadratic curve obtained by secondary fitting of the flow velocity curve of supercritical CO_2 in a 6 nm pore of kaolinite under different driving forces in Figure 3.8 are shown in Table 3.1. As can be seen from the table, the absolute value of the quadratic coefficient a of the quadratic curve gradually increases with the increase of the driving force, indicating that the velocity gradient in the z-axis direction of the velocity in the y direction gradually increases. From Figure 3.8, it can also be seen that the velocity of CO_2 molecules at the wall is not zero, which proves the existence of slip boundary and slip length.

Tab. 3.1 Fitting of Quadratic Curves for Different Driving Forces in 6nm Pores of Kaolinite

f (kcal/mol/Å)	a	b	c
0.0008	-1.50E-06	1.12E-04	-1.22E-03
0.0009	-1.70E-06	1.19E-04	-1.27E-03
0.0010	-1.80E-06	1.38E-04	-1.47E-03
0.0012	-2.10E-06	1.70E-04	-1.80E-03
0.0016	-2.90E-06	2.03E-04	-2.00E-03

For the flow of supercritical CO_2, the non-equilibrium molecular dynamics simulation was conducted to obtain the viscosity and slip length of the Poiseuille flow of the fluid under periodic boundary conditions. During the flow process, the boundaries were fixed, and a force f_y was applied to each atom in the +y direction of the fluid, according to the Alvarez pressure-driven mechanism. The equation of motion is given below:

$$\frac{d}{d_y}\left(\mu\frac{du_y}{d_z}\right)=-\rho f_y \tag{3.1}$$

Where u_y is the velocity in the y direction, ρ is the fluid density, and μ is the fluid viscosity. The equation can be further simplified as:

$$\mu=\frac{-\rho f_y}{d^2u_y/dz^2} \tag{3.2}$$

Based on the obtained quadratic flow curve, performing quadratic fitting, we get:

$$u_y=u_0+a(z-z_0)^2 \tag{3.3}$$

Where u_0, z_0 and a can be obtained by fitting the flow curve, and the viscosity can be calculated based on equations (3.2) and (3.3).

$$\mu=-\rho f_y/2a \tag{3.4}$$

The slip length is calculated using the Navier model:

$$L_s=\frac{V_{surf}}{(d_v/d_z)_{z_{surf}}} \tag{3.5}$$

where V_{surf} and $(d_v/d_z)_{z_{surf}}$ are the slip velocity and shear rate of the liquid at the solid-liquid interface. The positions of the upper and lower solid-liquid interfaces are defined as the positions of the bottom-most atom at the upper wall and the top-most atom at the lower wall, respectively. Parameters V_{surf} and $(d_v/d_z)_{z_{surf}}$ are obtained by fitting a parabolic curve to the velocity profile in the central region of the channel and extrapolating to the solid-liquid interface.

As shown in Figure 3.9, with the increase of the driving force, the viscosity of supercritical CO_2 remains almost unchanged, fluctuating within a small error range, indicating that the driving force has no effect on the flow viscosity of supercritical CO_2. The reason for the increase of slip length with the increase of driving force is analyzed as follows: the larger the driving force, the greater the change in the velocity of CO_2 molecules, which leads to a significant decrease in the CO_2 density in the adsorption layer. As a result, the CO_2 molecule density slightly increases outside the adsorption layer, causing the acceleration of the velocity gradient to decrease and the slip length to increase significantly.

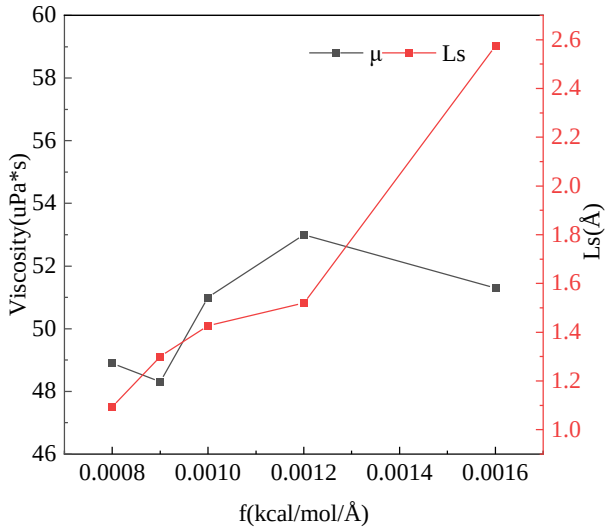

Fig. 3.9 Viscosity and slip length under different forces

3.2.2 Temperature effect on fluid flow

This section simulated the flow behavior of supercritical CO_2 in a 6 nm pore of kaolinite under a pressure of 20 MPa at temperatures of 350 K, 370 K, and 390 K, in order to investigate the changes in slip length, velocity distribution, and viscosity of supercritical CO_2 at the kaolinite wall at different temperatures.。

The effect of temperature on viscosity and slip length was investigated, and the results are shown in Figure 3.10. As the temperature increases, the slip length of supercritical CO_2 in the 6 nm pore of kaolinite gradually increases. The reason for the increasing slip length is that as the temperature increases, CO_2 molecules become more mobile, resulting in decreased stability, which in turn causes them to be more easily pushed, leading to increased slip length. The viscosity of supercritical CO_2 decreases with increasing temperature. By comparing the calculated viscosity at 350 K, 370 K, and

390 K with experimental data provided by NIST, the errors were found to be 0.02%, 4.59%, and 3.81%, respectively, which further validates the rationality of the flow model.

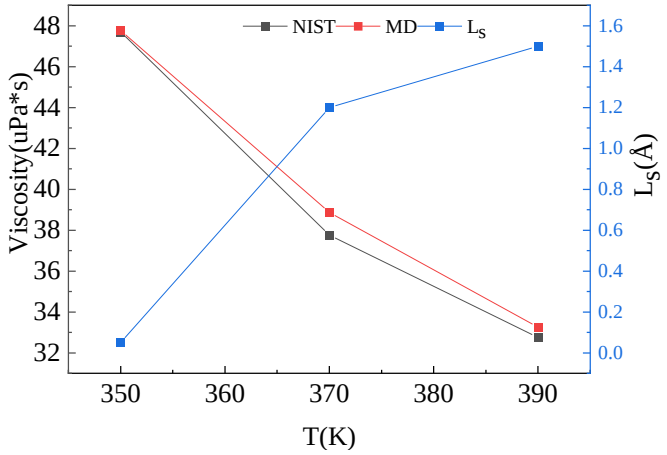

Fig. 3.10 Effect of Temperature on Flow Viscosity and Slip Length of kaolinite

From Figure 3.11, it can be seen that with the change of temperature, the curvature of the velocity parabolic curve changes. An increase in temperature leads to an increase in the curvature radius of the parabolic curve, while a decrease in temperature results in a decrease in the curvature radius. The velocity of CO_2 at the wall of the kaolinite undergoes a transition, which also has a certain impact on the slip length.

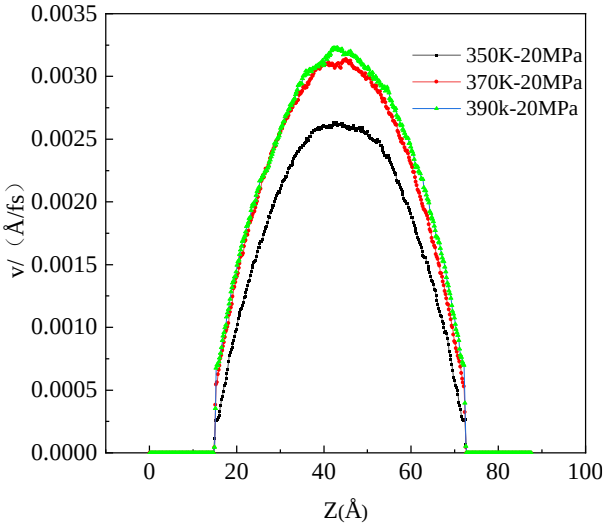

Fig. 3.11 Average Velocity Distribution of Carbon Dioxide at Different Temperatures in 6nm Porosity of kaolinite (350K)

3.2.3 Impact of pore size on flow

This section studied the effect of pore size on flow. The model directly used the final adsorption configurations of the 2 nm, 4 nm, and 6 nm pores of kaolinite in 350 K and 20 MPa. The driving force was based on the driving force of the 6 nm pore cross-section at 20 MPa pressure, which was 0.002087 kcal/mol/Å. The driving forces for the 2 nm and 4 nm pores were calculated and are listed in Table 3.2.

Tab. 3.2 Corresponding driving forces of different pores of kaolinite

Pore size(nm)	A_{xz}(nm^2)	f(kcal/mol/Å)
2nm	8.4	0.002130
4nm	16.8	0.002144
6nm	25.2	0.002087

The comparison of the flow density curves of supercritical CO_2 in different pore sizes of kaolinite is shown in Figure 3.12. The flow process is similar to the static process, with two adsorption layers appearing in all 2 nm, 4 nm, and 6 nm pores. The peak of the adsorption layer in the 2 nm pore is larger than that in the 4 nm and 6 nm pores. The peaks of the adsorption layer in the 4 nm and 6 nm pores are basically the same. This phenomenon indicates that the effect of the kaolinite wall potential on the 2 nm pore is still significant during the flow process, while the effect of the kaolinite wall in the 4 nm and 6 nm pores is the same. These phenomena indicate that the non-equilibrium molecular dynamics and Monte Carlo adsorption simulation show similar changes in the adsorption and flow density curves of CO_2 in different pores of kaolinite. The density peak at the kaolinite pore wall is reduced to varying degrees compared to the static adsorption process. Through quantitative analysis of this desorption phenomenon, the static density distribution of CO_2 in the 2 nm, 4 nm, and 6 nm pores was calculated to be 1.63 g/cm^3, 1.45 g/cm^3, and 1.42 g/cm^3, respectively. The peak density of the CO_2 after flow is reduced to 1.51 g/cm^3, 1.28 g/cm^3, and 1.13 g/cm3, respectively, representing a decrease of 7.95%, 11.72%, and 20.42%. This indicates that the driving force causes the adsorbed CO_2 molecules at the pore wall to desorb, and the desorption phenomenon becomes more pronounced as the pore size increases. The density peak of the first adsorption layer decreases in all pores, while the density of the second adsorption layer remains basically unchanged, leading to an increase in the density of the free layer CO_2.

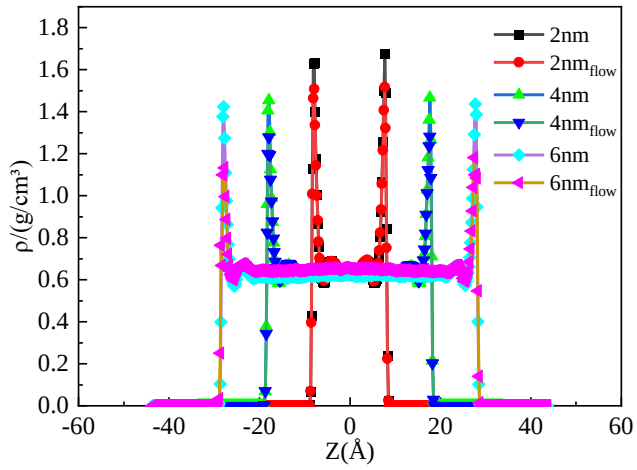

Fig. 3.12 Curve of Carbon Dioxide Adsorption and Flow Density in Different Pores of kaolinite (350K-20MPa)

As the pore size increases, the reduction in the density of the first adsorption layer also increases. To explore the reason behind this, the relationship between the velocity of supercritical CO_2 and pore size was further analyzed, and the results are shown in Figure 3.13. As shown in the figure, with the continuous increase of the pore size of the kaolinite, the decrease in the density of the adsorption layer reduces the resistance to CO_2 flow during the flow process, leading to an increase in the velocity of supercritical CO_2 in the adsorption layer. This effect becomes more significant as the pore size increases, and the increase in velocity makes CO_2 molecules move more violently, increasing the chance of molecular collisions and ultimately leading to desorption of CO_2 molecules in the adsorption layer. At the same time, with the increase of pore size, the velocity of supercritical CO_2 molecules at the kaolinite surface undergoes a transition, which is positively correlated with the pore size. Based on the combined density and velocity change curves, it can be concluded that the degree of CO_2 desorption is directly proportional to the molecular velocity change.

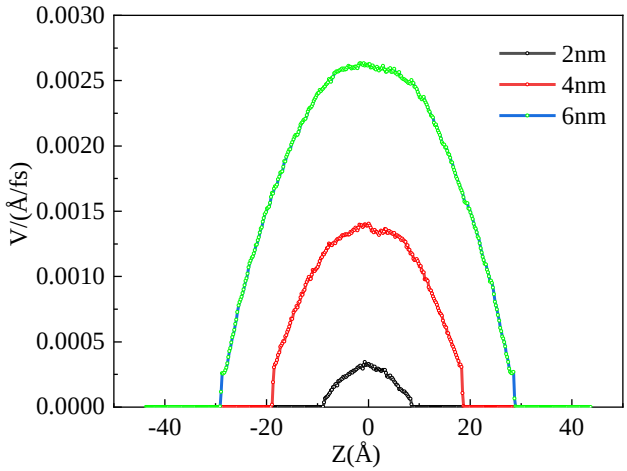

Fig. 3.13 Supercritical Carbon Dioxide Flow Rate Curve of kaolinite with Different Porosity

The curve of the supercritical CO_2 velocity in Figure 3.13 was fitted, and the parameters are shown in Table 3.3. As shown in the table, with the increase of the pore size, the absolute value of the curvature a of the quadratic curve gradually decreases. This indicates that the absolute value of the velocity gradient at the wall decreases with the increase of pore size. During the flow process, the significant decrease in adsorption layer density with the increase of pore size leads to a significant change in adsorption layer velocity. However, the density of free CO_2 molecules in the bulk phase only undergoes a small change, which causes the velocity of free CO_2 molecules in the bulk phase to also undergo a small change. Therefore, within the same pore, the velocity gradient changes gradually decrease along the Z direction from the wall to the center of the pore. With the increase of pore size, the changes in velocity gradient along the Z direction from the surface of the kaolinite to the center of the pore also gradually decrease.

Pores(nm)	a	b	c
2nm	-1.3782E-6	-2.54387E-9	1.09742E-4
4nm	-1.3316E-6	-1.5329E-7	4.8538E-4
6nm	-1.28223E-6	-3.52409E-7	0.00121

4. DISCUSSION

The effects of pressure, temperature, and pore size on the adsorption of CO_2 on kaolinite were analyzed through isothermal adsorption curves, density curves, and potential of mean force (PMF) calculations. With the increase of pressure, the total amount of CO_2 adsorbed in the kaolinite pores showed a rapid increase followed by a gradual saturation trend. The slope of the isothermal adsorption curve increased first and then

decreased, while the PMF decreased overall with increasing pressure and eventually stabilized near the PMF value corresponding to 30 MPa.

As the temperature increases, the total amount of CO_2 molecules adsorbed on kaolinite decreases. Analysis of the adsorption density curve shows that increasing the temperature not only reduces the density of the adsorption layer, but also significantly reduces the density of the free state, leading to desorption of CO_2. The potential energy distribution at different temperatures shows that the potential energy increases with temperature, and the corresponding distribution of the number of potential energy states indicates that the number of adsorbed and free CO_2 molecules decreases with increasing temperature, but the decrease in the number of free CO_2 molecules is more pronounced.

As the pore size gradually increases, under 350 K conditions, the amount of CO_2 adsorption in each group of pores shows a trend of gradually increasing and then approaching saturation as the pressure increases. This can be seen from the corresponding adsorption isotherm curves, and in the corresponding density curves, the peak of the adsorption density curve of 1 nm and 2 nm pores is larger than that of 4 nm and 6 nm pores. Only one adsorption layer exists in the 1 nm pore, and CO_2 molecules in the pore exist in an adsorbed state, while two adsorption layers appear in the 2 nm, 4 nm, and 6 nm pores under 350 K and 20 MPa temperature and pressure conditions. CO_2 molecules in the pore, except for those in the adsorption layer, exist in a free state. From the potential Poisson distribution of the pores, the 1 nm pore has only a single potential peak, and the potential value is smaller than that of other pores, resulting in a higher adsorption amount. This is because the 1 nm pore is subject to the double overlapping effect of the potential on both sides of the wall, resulting in a decrease in potential and an increase in adsorption amount.

Based on the adsorption simulation, the flow behavior of supercritical CO_2 in the kaolinite-supercritical CO_2 model was studied. The effects of driving force, temperature, and pore size on flow were analyzed. The following conclusions were drawn:

The magnitude of the driving force directly affects the adsorption state of supercritical CO_2 on the surface of kaolinite. As the driving force increases, the adsorption peak on the surface of kaolinite gradually decreases, and the peak reduction is greater with increasing driving force. The velocity distribution of supercritical CO_2 follows a Poisson distribution, with the velocity decreasing from the center of the pore to the two walls, due to the strong adsorption of CO_2 molecules by the wall. This effect can be indirectly reflected by the distribution of carbon atom potential energy in the 6 nm pore of kaolinite. The potential energy distribution shows that the first adsorption layer near the wall has the lowest energy, indicating strong adsorption, while the potential energy of the second adsorption layer is greater than that of the first but less than that of the free layer, indicating weak adsorption. The potential energy of the carbon atom in the free layer is close to zero, indicating that supercritical CO_2 molecules far from the pore wall are hardly affected by the wall. The wall adsorption effect acts as resistance in the flow process, causing the CO_2 flow velocity near the wall to be lower than that near the center of the pore. The velocity at the wall is not zero, which indicates that the continuity hypothesis of fluid mechanics is no longer applicable at the micro level. The slip length of supercritical CO_2 is obtained by fitting the quadratic curve of the velocity, which gradually increases with the increase of the driving force. The average velocity of supercritical CO_2 is proportional to the driving force and follows Darcy's law within the range of 0.0008-0.0016 kcal/mol/Å.

In the process of supercritical CO_2 flow, temperature also has a significant impact on its viscosity, density, and slip length. As the temperature increases, the overall density of CO_2 decreases significantly. Due to the increased temperature, CO_2 molecules move more violently, leading to desorption from the high-alumina clay surface. Weakened surface adsorption reduces the resistance in the flow process, which manifests as a decrease in the viscosity of supercritical CO_2 at the macro level and an increase in slip length.

Under 350 K and 20 MPa temperature and pressure conditions, the interaction force in different pores was calculated based on the 6 nm pore, and the flow density and adsorption density curves in different pores were compared. As the pore size increases, desorption occurs more prominently at the high-alumina surface during the flow process. The velocity distribution curve for larger pores exhibits a larger curvature, which leads to a more significant change in velocity of supercritical CO_2 molecules, intensifying their collisions and weakening the adsorption effect on the wall surface, resulting in reduced resistance to flow and lower viscosity. This causes an increase in the average velocity of supercritical CO_2.

5. CONCLUSIONS

In the geological storage process, the pore size and structure of the reservoir are crucial factors affecting the effectiveness of CO_2 sequestration in the supercritical state. Clay minerals have a large specific surface area and many adsorption sites, which play a significant role in the adsorption process. Moreover, clay minerals have the advantages of low adsorption cost and natural abundance. Therefore, considering the pore size and structure of the reservoir and the characteristics of clay minerals is essential in the reservoir selection process. In this study, the characteristics of the high-alumina clay pore wall were investigated using Monte Carlo methods and molecular dynamics, and the effects of pore size and structure on CO_2 sequestration were comprehensively analyzed from the perspectives of adsorption and flow. The study was conducted in several parts: (a) analyzing the main factors affecting CO_2 adsorption in detail, including pressure, temperature, and pore size; (b) exploring the flow state of supercritical CO_2 from the perspectives of driving force, temperature, and pore size. Through a series of simulation studies, the interfacial characteristics of the high-alumina clay-CO_2 multiphase system and the flow rules of supercritical CO_2 were obtained. The conclusions are as follows:

(1) When the temperature is fixed at 350K, as the pressure gradually increases, the amount of CO_2 adsorption increases and eventually reaches saturation. As the pressure increases, the CO_2 potential energy decreases, and when the pressure reaches 30 MPa and 35 MPa, the CO_2 potential energy no longer changes, further indicating that adsorption has reached saturation.

(2) Temperature not only affects CO_2 adsorption in the adsorption layer, but also has a significant impact on free CO_2. From the isothermal adsorption curve, increasing the temperature reduces the amount of CO_2 adsorption, indicating that heating is a way of CO_2 desorption. The main reason for this is that the increase in temperature causes the potential energy of CO_2 molecules to increase, making them less likely to be adsorbed. Cooling reduces the potential energy of CO_2 molecules, increasing the amount of CO_2 adsorption.

(3) The amount of CO_2 adsorption in 1 nm pores is significantly higher than in other pores. This is because in smaller pores, CO_2 is subject to the overlapping effects of adsorption on both sides of the kaolinite walls, resulting in a significantly higher adsorption layer density. From the potential energy distribution perspective, the CO_2 potential energy in 1 nm pores is lower than in other pores, resulting in more CO_2 being adsorbed on the kaolinite walls.

(4) As the driving force gradually increases, the density of the CO_2 adsorption layer gradually decreases but the adsorption phenomenon still exists. The curvature radius of the velocity curve gradually increases, and the velocity at the wall is not zero, indicating the existence of slip phenomenon during the flow of supercritical CO_2.

(5) The effect of temperature on the flow process is mainly reflected in the viscosity and slip length of supercritical CO_2. With increasing temperature, the curvature radius of the velocity distribution curve of supercritical CO_2 increases, the density decreases, and at the same time, the viscosity decreases. With increasing temperature, CO_2 molecules move more violently, making them more prone to desorption and more easily driven, resulting in an increase in slip length.

(6) As the pore size increases, the peak of the adsorbed CO_2 layer decreases when the driving force is applied to the supercritical CO_2 in the pore. The larger the pore, the greater the decrease in adsorption layer density. Combined with the CO_2 velocity distribution curve, the larger the pore, the faster the CO_2 velocity, and the more violent the molecular movement, making CO_2 less stable and more prone to desorption. This also explains the reason for the degree of CO_2 desorption increasing with increasing pore size. Fitting the change in CO_2 velocity with the applied force for different pores, due to the significant effect of kaolinite wall potential energy in 2 nm pores, CO_2 experiences greater resistance from the walls, resulting in a smaller average velocity. As the pore size increases, the wall effect weakens, and the CO_2 velocity increases significantly, resulting in supercritical CO_2 flow in different pores no longer following Darcy's law.

ACKNOWLEDGEMENT

THIS PAPER WAS SUPPORTED BY THE NATIONAL NATURAL SCIENCE FOUNDATION OF CHINA (GRANT 51976024), LIAONING REVITALIZATION TALENTS PROGRAM (GRANT XLYC2007117), AND THE FUNDAMENTAL RESEARCH FOR APPLICATION OF LIAONING PROVINCE (GRANT 2023JH2/101300005).

DECLARATION OF INTEREST STATEMENT

The authors declare that they have no known competing financial interests or personal relationships

that could have appeared to influence the work reported in this paper. All authors read and approved the final manuscript.

REFERENCE

[1] Y. Ou, C. Roney, J. Alsalam, K. Calvin, J. Creason, J. Edmonds, A.A. Fawcett, P. Kyle, K. Narayan, P. O'Rourke, P. Patel, S. Ragnauth, S.J. Smith, H. McJeon, Deep mitigation of CO_2 and non-CO_2 greenhouse gases toward 1.5 degrees C and 2 degrees C futures, Nat. Commun. (2021) 12(1) 9. https://doi.org/10.1038/s41467-021-26509-z.

[2] A. Ilinova, E. Kuznetsova, CC(U)S initiatives: Prospects and economic efficiency in a circular economy, Energy Rep.(2022) 8 1295-1301. https://doi.org/10.1016/j.egyr.2021.11.243.

[3] A.D.N. Kamkeng, M.H. Wang, J. Hu, W.L. Du, F. Qian, Transformation technologies for CO_2 utilisation: Current status, challenges and future prospects, Chem. Eng. J. (2021) 409 29. https://doi.org/10.1016/j.cej.2020.128138.

[4] A. Kumar, N. Daraboina, R. Kumar, P. Linga, Experimental Investigation To Elucidate Why Tetrahydrofuran Rapidly Promotes Methane Hydrate Formation Kinetics: Applicable to Energy Storage, Journal of Physical Chemistry C (2016) 120(51) 29062-29068. https://doi.org/10.1021/acs.jpcc.6b11995.

[5] D.L. Bish, RIETVELD REFINEMENT OF THE KAOLINITE STRUCTURE AT 1.5-K, Clay Clay Min. (1993) 41(6) 738-744. https://doi.org/10.1346/ccmn.1993.0410613.

[6] W.D. Gunter, T. Gentzis, B.A. Rottenfusser, R.J.H. Richardson, Deep coalbed methane in Alberta, Canada: A fuel resource with the potential of zero greenhouse gas emissions, Energy Conv. Manag. (1997) 38 S217-S222. https://doi.org/10.1016/s0196-8904(96)00272-5.

[7] R.K. Saran, V. Arora, S. Yadav, CO_2 sequestration by mineral carbonation: a review, Glob. Nest. J. (2018) 20(3) 497-503. https://doi.org/10.30955/gnj.002597.

[8] C. McDermott, J. Williams, O. Tucker, M. Jin, E. Mackay, K. Edlmann, R.S. Haszeldine, W.Q. Wang, O. Kolditz, M. Akhurst, Screening the geomechanical stability (thermal and mechanical) of shared multi-user CO_2 storage assets: A simple effective tool applied to the Captain Sandstone Aquifer, International Journal of Greenhouse Gas Control (2016) 45 43-61. https://doi.org/10.1016/j.ijggc.2015.11.025.

[9] D.D. Li, X. Jiang, Q.L. Meng, Q.Y. Xie, Numerical analyses of the effects of nitrogen on the dissolution trapping mechanism of carbon dioxide geological storage, Comput. Fluids (2015) 114 1-11. https://doi.org/10.1016/j.compfluid.2015.02.014.

[10] S. Fakher, M. Ahdaya, M. Elturki, A. Imqam, An experimental investigation of asphaltene stability in heavy crude oil during carbon dioxide injection, Journal of Petroleum Exploration and Production Technology (2020) 10(3) 919-931. https://doi.org/10.1007/s13202-019-00782-7.

[11] S.J. Fuchs, D.N. Espinoza, C.L. Lopano, A.-T. Akono, C.J. Werth, Geochemical and geomechanical alteration of siliciclastic reservoir rock by supercritical CO_2-saturated brine formed during geological carbon sequestration, International Journal of Greenhouse Gas Control (2019) 88 251-260. https://doi.org/10.1016/j.ijggc.2019.06.014.

[12] X. Guo, H. Ni, M. Li, L. Zhang, Y. Wang, L. Ding, Experimental Study on the Influence of Supercritical Carbon Dioxide Soaking Pressure on the Mechanical Properties of Shale, Indian Geotechnical Journal (2018) 48(2) 384-391. https://doi.org/10.1007/s40098-017-0289-8.

[13] S. Khan, Y.A. Khulief, A. Al-Shuhail, Mitigating climate change via CO_2 sequestration into Biyadh reservoir: geomechanical modeling and caprock integrity, Mitigation and Adaptation Strategies for Global Change (2019) 24(1) 23-52. https://doi.org/10.1007/s11027-018-9792-1.

[14] P. Chenrai, S. Jitmahantakul, R. Bissen, T. Assawincharoenkij, A preliminary assessment of geological CO_2 storage in the Khorat Plateau, Thailand, Front. Energy Res. (2022) 10 20. https://doi.org/10.3389/fenrg.2022.909898.

[15] J. Dubinski, A. Koteras, Possibilities of CO_2storage in geological formations, Energetyka (Poland) (2014) (1) 20-24.

[16] F.S. Han, X.L. Wu, Numerical simulation of compressive experiment of Coal Seam in deep underground for geological storage of carbon dioxide, International Conference on Applied Mechanics, Materials and Mechanical Engineering (AMME 2013), Trans Tech Publications Ltd, Wuhan, PEOPLES R CHINA, 2013, pp. 189-+.

[17] D.J.K. Ross, R.M. Bustin, The importance of shale composition and pore structure upon gas storage potential of shale gas reservoirs, Mar. Pet. Geol. (2009) 26(6) 916-927. https://doi.org/10.1016/j.marpetgeo.2008.06.004.

[18] C.E. WHTTE, J.L. PROVIS, D.P. RILEY, What Is t he Structure of Kaolinite Reconciling Theory and Ex periment, The Joumal of Physical Chemistry B (200 9) 113(19) 6756-6765.
[19] R.A. Young, A.W. Hewat, VERIFICATION OF THE TRICLINIC CRYSTAL-STRUCTURE OF KAOLINITE, Clay Clay Min. (1988) 36(3) 225-232. https://doi.org/10.1 346/ccmn.1988.0360303.
[20] R.T. Cygan, J.J. Liang, A.G. Kalinichev, Molecula r models of hydroxide, oxyhydroxide, and clay phas es and the development of a general force field, J ournal of Physical Chemistry B (2004) 108(4) 1255- 1266. https://doi.org/10.1021/jp0363287.
[21] J. G., Harris., K.H. Yung, Carbon Dioxide's Liqui d-Vapor Coexistence Curve and Critical Properties A s Predicted, American Chemical Society (1995) 99(3 1) 12012-12024.